



# Amorphous $\text{NiSb}_2\text{O}_{6-x}$ nanofiber: A $d$ -/ $p$ -block Janus electrocatalyst toward efficient $\text{NH}_3$ synthesis through boosted $\text{N}_2$ adsorption and activation

Wanping Xu<sup>a</sup>, Meng Zhang<sup>a</sup>, Chunlan Ma<sup>b</sup>, Shuhong Wu<sup>c,d</sup>, Yi-Tao Liu<sup>a,\*</sup>

<sup>a</sup> Innovation Center for Textile Science and Technology, Donghua University, Shanghai 201620, China

<sup>b</sup> Jiangsu Key Laboratory of Micro and Nano Heat Fluid Flow Technology and Energy Application, School of Physical Science and Technology, Suzhou University of Science and Technology, Suzhou 215009, China

<sup>c</sup> School of Materials Science and Engineering, Shanghai Jiao Tong University, Shanghai 200240, China

<sup>d</sup> National Engineering Research Center for Nanotechnology, Shanghai 200240, China

## ARTICLE INFO

### Keywords:

Amorphous nanofiber  
 $d$ -block element  
 $p$ -block element  
Janus electrocatalyst  
 $\text{N}_2$  reduction reaction

## ABSTRACT

The electrochemical  $\text{N}_2$  reduction reaction (NRR) is greatly challenged by relatively low faradaic efficiency (FE) owing to fierce competition from the  $\text{H}_2$  evolution reaction (HER) suffered by the current transition-metal electrocatalysts ( $d$ -block elements). Considering the unique electronic structure of group-VA pnictogens ( $p$ -block elements) that is complementary to  $d$ -block elements in HER suppression, we report a conceptually new Janus electrocatalyst to tackle the selectivity challenge. Specifically, an amorphous  $\text{NiSb}_2\text{O}_{6-x}$  nanofiber is synthesized, in which Ni and Sb contribute to a synergistic catalysis pathway for inhibiting the two-electron transfer process of HER as well as activating the adsorbed  $\text{N}_2$  molecules. Moreover, amorphization is able to produce more oxygen vacancies, thus mimicking the “ $\pi$  back-donation” process to promote the NRR performance. Benefiting from this coupled element design and amorphization strategy, the amorphous  $\text{NiSb}_2\text{O}_{6-x}$  nanofiber significantly outperforms either component ( $\text{NiO}$  or  $\text{Sb}_2\text{O}_4$ ) as well as its crystalline counterparts in terms of  $\text{NH}_3$  yield and FE.

## 1. Introduction

$\text{NH}_3$  is an essential nitrogen feedstock widely used in modern agricultural, chemical and pharmaceutical industries. It also serves ideally as an energy storage intermediate and a carbon-free energy carrier. The current  $\text{NH}_3$  production is over 200 million tons annually, mainly relying on the energy-intensive Haber–Bosch process under high temperature and pressure [1]. As such, ca. 1–2% anthropogenic energy is consumed each year to meet the global  $\text{NH}_3$  demand, accompanied by the emission of significant levels of greenhouse gas ( $\text{CO}_2$ ) [2]. In this context, the electrocatalytic  $\text{N}_2$  reduction reaction (NRR) has come to the researchers' attention as a clean and energy-efficient alternative for  $\text{N}_2$  fixation, since it can be operated under ambient conditions. However, the  $\text{NH}_3$  yield and faradaic efficiency (FE) of electrocatalytic NRR are still unsatisfactory owing to the thermodynamical stability of the  $\text{N}\equiv\text{N}$  bond and the serious competition from the  $\text{H}_2$  evolution reaction (HER) [3]. Therefore, it is of utmost importance to explore electrocatalysts with reasonably high activity and selectivity to promote  $\text{N}_2$  adsorption and activation [4].

As revealed theoretically, the unoccupied  $d$  orbital of transition metals (TMs, also known as  $d$ -block elements) is accessible to the lone-pair electrons of  $\text{N}_2$  ( $\sigma$  donation), and the separated  $d$ -orbital electrons can be fed back to the  $\pi^*$  orbital of  $\text{N}_2$  ( $\pi$  back-donation), thereby weakening the  $\text{N}\equiv\text{N}$  bond while strengthening the  $\text{TM}-\text{N}$  bond to facilitate  $\text{N}_2$  activation [5]. Thus far, a wide variety of TM species have been investigated as possible NRR electrocatalysts. The earliest researches mainly concentrated on precious metals such as Ru [6,7], Rh [8], and Pt [9]. In light of their unrealistically high costs, the research focuses gradually shifted to non-precious metal compounds such as chalcogenide [10–14], nitride [15–17], oxide [18–20], and carbide [21–23]. Note that the NRR activity of these compounds was far below expectations since they were mantled by the electronegative atoms, and the metal atoms were overwhelmingly shielded. Therefore, several strategies were proposed to expose the metal atoms as active centers by creating defects [24,25]. For example, strain-induced anion vacancies could be formed by lattice doping [26–30] or micromechanical friction [31]. Besides, chemical [32] or thermal reduction [33,34] was another way of creating anion vacancies. However, the improvement in NRR

\* Corresponding author.

E-mail address: [liu-yt03@dhu.edu.cn](mailto:liu-yt03@dhu.edu.cn) (Y.-T. Liu).

<https://doi.org/10.1016/j.apcatb.2022.121225>

Received 10 December 2021; Received in revised form 6 February 2022; Accepted 15 February 2022

Available online 18 February 2022

0926-3373/© 2022 Elsevier B.V. All rights reserved.

activity was still undermined by the limited vacancy contents generated in these highly crystalline electrocatalysts.

On the other hand, it is disclosed by the volcano plot that high activity and selectivity are hard to be achieved simultaneously according to the scaling relations of the adsorption energies of NRR intermediates [35]. Generally, TMs suffer from relatively low NRR selectivity owing to serious competition from HER arising from strong binding between the unoccupied *d* orbital and the H adatoms [36]. In this regard, group-VA pnictogens (also known as *p*-block elements) have attracted increasing attention owing to their unique electronic structure similar to that of N, as well as their inferior HER activity. For example, Bi was found to be a promising candidate for high-selectivity NRR since it could bind more strongly with N<sub>2</sub> than with H<sub>2</sub> [37–39]. Besides, the NRR performance of P was explored in our previous work, which also exhibited higher NRR selectivity than TMs by effectively suppressing HER [40,41]. It should be noted, however, that the NRR activity of pnictogens was rather disappointing in most cases because of the lack of unoccupied orbital to mimic the “ $\pi$  back-donation” behavior [42].

In light of the distinct yet complementary electronic structures of *d*- and *p*-block elements, here we report a conceptually new Janus electrocatalyst, *i.e.*, an amorphous NiSb<sub>2</sub>O<sub>6-x</sub> nanofiber. As a representative *d*-block element, Ni is used as the active species owing to its capacity in N<sub>2</sub> activation and H<sub>2</sub>O dissociation [43]. However, the selectivity of Ni-based electrocatalysts has much scope to be improved on account of the affinity of H adatoms with Ni, leading to intense competition from HER [44]. As such, it is integrated with a *p*-block element Sb which was theoretically predicted to be able to inhibit the two-electron transfer process of HER [45,46]. To further promote the NRR performance, a new strategy of amorphization is developed which is expected to produce more oxygen vacancies (OVs) and under-coordinated dangling bonds to mimic the “ $\pi$  back-donation” behavior [47]. Benefiting from this coupled element design and amorphization strategy, the amorphous NiSb<sub>2</sub>O<sub>6-x</sub> nanofiber outperforms either component (NiO or Sb<sub>2</sub>O<sub>4</sub>) as well as its crystalline counterparts in terms of NH<sub>3</sub> yield and FE, whose underlying mechanism is explored by means of density functional theory (DFT) calculations. In this sense, our work represents a successful attempt to design efficient electrocatalysts for NH<sub>3</sub> synthesis.

## 2. Experimental section

### 2.1. Materials

SbCl<sub>3</sub>, Ni(CH<sub>3</sub>COO)<sub>2</sub>·4H<sub>2</sub>O, polyvinylpyrrolidone (PVP, *M<sub>w</sub>* = 1,300,000), and NH<sub>4</sub>Cl were purchased from Shanghai Aladdin Biochemical Technology Co., Ltd. Ethanol, *N,N*-dimethylformamide (DMF), and HCl were purchased from Shanghai Titan Scientific Co., Ltd. Citric acid, sodium salicylate, and sodium nitroprusside dihydrate were purchased from Shanghai Macklin Biochemical Co., Ltd. Na<sub>2</sub>SO<sub>4</sub> and NaClO were purchased from Shanghai Rhawn Chemical Reagent Co., Ltd. Ni foam was purchased from Changde Liyuan New Material Co., Ltd. Nafion 211 membrane was purchased from Shanghai Jing Chong Electronic Technology Development Co., Ltd. N<sub>2</sub> and Ar were purchased from Air Liquide (Shanghai) Co., Ltd. <sup>15</sup>N<sub>2</sub> was purchased from Wuhan Newradar Special Gas Co., Ltd.

### 2.2. Synthesis of amorphous NiSb<sub>2</sub>O<sub>6-x</sub> nanofiber

Firstly, 0.96 g of citric acid was dissolved in a mixed solvent of ethanol (20 mL) and *N,N*-dimethylformamide (DMF, 20 mL) under vigorous stirring for 1 h. Then, 1.82 g of SbCl<sub>3</sub>, 0.99 g of Ni(CH<sub>3</sub>COO)<sub>2</sub>·4H<sub>2</sub>O, and 2.7 g of PVP were added to the above solution. The mixed solution was stirred for 12 h at room temperature to obtain a precursor solution, which was transferred into a syringe and electrospun by using a DXES-1 electrospinning equipment. The electrospinning parameters were as follows: an applied voltage of 15 kV, a receiving distance of 15 cm, and a perfusion speed of 0.8 mL h<sup>-1</sup>. During the

electrospinning process, the temperature was maintained at 22 ± 2 °C and the humidity was kept at ca. 40%. Finally, the as-spun nanofiber was calcinated at 560 °C in air for 60 min at a heating rate of 2 °C min<sup>-1</sup> to obtain an amorphous NiSb<sub>2</sub>O<sub>6-x</sub> (denoted as *a*-NiSb<sub>2</sub>O<sub>6-x</sub>) nanofiber. For comparison, the as-spun nanofiber was calcinated at 600 or 700 °C to obtain a partially crystalline or crystalline NiSb<sub>2</sub>O<sub>6-x</sub> (denoted as *pc*-NiSb<sub>2</sub>O<sub>6-x</sub> or *c*-NiSb<sub>2</sub>O<sub>6-x</sub>) nanofiber.

### 2.3. Characterization

The scanning electron microscopy (SEM) was carried out by a Hitachi S-4800 microscope. The transmission electron microscopy (TEM) and high-resolution TEM (HRTEM) were carried out by a Talos F200S microscope. The X-ray diffraction (XRD) spectroscopy was carried out by a Bruker D8 Advance diffractometer with Cu K $\alpha$  radiation ( $\lambda$  = 1.5405 Å). The thermogravimetric analysis (TGA) was carried out by a TA-SDT Q600 analyzer. The Brunauer–Emmett–Teller (BET) surface area was measured by a Micromeritics ASAP 2040 analyzer at 77 K. The electron paramagnetic resonance (EPR) spectroscopy was carried out by a Bruker EMX-8 spectrometer at 9.44 GHz at 300 K. The Raman spectroscopy was carried out by a LabRAM HR Evolution spectrometer. The X-ray photoelectron spectroscopy (XPS) was carried out by a ULVAC-PHI Quantera SXM spectrometer. The N<sub>2</sub> temperature-programmed desorption (N<sub>2</sub>-TPD) measurement was carried out by an Autosorb-iQ-C chemisorption analyzer. The <sup>1</sup>H nuclear magnetic resonance (NMR) spectroscopy was carried out by a Bruker AV Neo500 spectrometer with a cryogenic probe. The electrochemical measurement was carried out by a Bio-Logic VSP workstation. The UV–vis spectroscopy was carried out by a Hitachi U-3900 spectrophotometer.

### 2.4. Electrochemical measurement

Typically, the electrocatalyst (15 mg) was added to a mixture of 5 wt % Nafion solution (300  $\mu$ L) and ethanol (1200  $\mu$ L), and then sonicated for 4 h to obtain a homogeneous ink. A Ni foam was tailored into 1 × 1 cm<sup>2</sup> pieces and treated in acetone, 1 M HCl, ethanol and deionized water one by one (all kept for 30 min) to remove the impurities. The ink (100  $\mu$ L) was pipetted onto each piece of Ni foam and used as the working electrode. A saturated calomel electrode (SCE) was used as the reference electrode, and a Pt mesh was used as the counter electrode. A Nafion 211 membrane was pre-treated in 5% H<sub>2</sub>O<sub>2</sub> for 20 min, deionized water for 20 min, and 0.5 M H<sub>2</sub>SO<sub>4</sub> for 20 min (room temperature), and in deionized water at 80 °C for more than 12 h under sonication. It was then used to separate a two-compartment electrocatalysis cell under ambient conditions, in which the electrochemical measurement was carried out. The electrolyte in each compartment was 50 mL. Before the experiment, the electrocatalysis cell was sealed, and the feed gas (99.999% N<sub>2</sub>) was introduced into the electrolyte for at least 30 min after passing through KOH (pH = 13) and H<sub>2</sub>SO<sub>4</sub> (pH = 1). The chronoamperometric curves were recorded at different potentials for 2 h by using an electrochemical workstation, and all potentials were converted to the reversible hydrogen electrode (RHE). The concentration–absorbance curves of NH<sub>3</sub>, N<sub>2</sub>H<sub>4</sub> and NO<sub>2</sub><sup>-</sup> were calibrated by using standard NH<sub>3</sub>, N<sub>2</sub>H<sub>4</sub> and NaNO<sub>2</sub> solutions at a series of concentrations, respectively. The concentrations of NH<sub>3</sub>, N<sub>2</sub>H<sub>4</sub> and NO<sub>2</sub><sup>-</sup> were determined by the above concentration–absorbance curves according to the details specified in our previous work [40].

### 2.5. DFT calculations

First-principles calculations were carried out by using DFT with generalized gradient approximation (GGA) of Perdew–Burke–Ernzerhof (PBE) implemented in the Vienna Ab-Initio Simulation Package (VASP) [48,49]. The valence electronic states were expanded on the basis of plane waves with the core-valence interaction represented by using the projector augmented plane wave (PAW) approach and a cutoff value of

450 eV [50]. The Brillouin zone integration was sampled with  $2 \times 2 \times 1$  K-point meshes for geometry optimization. The structures were fully relaxed until the maximum force on each atom became less than  $0.02 \text{ eV } \text{\AA}^{-1}$ . The surface models were cleaved from the optimized bulk structures with a vacuum thickness of  $15 \text{ \AA}$  to suppress the interaction between adjacent slabs. A  $2 \times 2$  supercell with 15 at. layers was used in our calculations. To mimic different crystalline systems, we considered three different systems with 5%, 15% and 25% randomly distributed vacancies. The adsorption energy of adsorbed species was calculated as formula 1:

$$\Delta E_{\text{ad}} = E_{\text{substrate+adsorbate}} - E_{\text{substrate}} - E_{\text{adsorbate}} \quad (1)$$

where  $E_{\text{substrate+adsorbate}}$ ,  $E_{\text{substrate}}$  and  $E_{\text{adsorbate}}$  were the total energies of the whole system, the substrate and the adsorbed species, respectively.

### 3. Results and discussion

#### 3.1. Formation mechanism and characterization of amorphous $\text{NiSb}_2\text{O}_{6-x}$ nanofiber

The  $\alpha\text{-NiSb}_2\text{O}_{6-x}$  nanofiber with rich OVVs is rationally synthesized through a multifunctional PVP-mediated process, as depicted in Fig. 1. PVP is a long-chain polymer containing large quantities of lactam rings, which have inherently different interactions with metal cations and the solvent in a complex liquid or solid state. At first, citric acid is used as a chelating agent to coordinate with metal cations, and it also favors an increase in the  $\text{H}^+$  donor, whereupon the  $\text{C}=\text{O}$  groups and N atoms of PVP are more likely to form H bonds [51]. Thus, a stable and homogeneous precursor solution with proper viscosity can be prepared owing to the electronic effect among the lactam rings of PVP, metal cations and carboxyl groups of citric acid. Furthermore, the homogeneity in the liquid state is maintained in the precursor nanofiber as much as possible

via rapid solvent evaporation during the electrospinning process. As the solvent evaporates and the metal–citrate complex decomposes during the calcination process in air, the resonance structures of the lactam rings of PVP offer two adsorption sites for the metal cations [52,53]. Meanwhile, the steric hindrance of PVP impedes the agglomeration and crystallization of metal cations. Therefore, the homogeneously distributed metal cations are almost stoichiometric in any local range of the nanofiber, and then directly form the  $\alpha\text{-NiSb}_2\text{O}_{6-x}$  nanofiber *in situ* with the complete decomposition of PVP. Owing to the slight non-stoichiometric defects and the lack of long-distance ordered state in the  $\alpha\text{-NiSb}_2\text{O}_{6-x}$  nanofiber, abundant OVVs and under-coordinated dangling bonds are created, which can facilitate  $\text{N}_2$  adsorption and activation.

Fig. S1 presents the TGA curve of the precursor nanofiber in air. The first weight loss below  $200^\circ\text{C}$  was ascribed to the evaporation of DMF, ethanol and  $\text{H}_2\text{O}$  in the as-spun nanofiber (region I). In the second weight loss, the metal–citrate complex began to decompose, meanwhile the residual solvent was decomposed completely (region II). As the temperature increased to ca.  $300^\circ\text{C}$  (region III-1), the thermal decomposition of the acetate groups and the degradation of the pyrrolidone groups in PVP occurred. The weight loss continued up to  $550^\circ\text{C}$ , which indicated that the unsaturated carbon backbone and residual organic compositions were burnt out and the remained material was pure  $\alpha\text{-NiSb}_2\text{O}_{6-x}$  (region III-2) [54]. At first, the morphology of the  $\alpha\text{-NiSb}_2\text{O}_{6-x}$  nanofiber was compared with that of the  $pc\text{-NiSb}_2\text{O}_{6-x}$  or  $c\text{-NiSb}_2\text{O}_{6-x}$  nanofiber, as presented in Fig. 2. Under SEM and TEM observation, the  $\alpha\text{-NiSb}_2\text{O}_{6-x}$  nanofiber exhibits a smooth surface and a compact inner structure (Figs. 2a and S2), probably owing to the slow decomposition of PVP during calcination at  $560^\circ\text{C}$  without causing agglomeration and crystallization of metal cations. The disordered state of the  $\alpha\text{-NiSb}_2\text{O}_{6-x}$  nanofiber can be identified by HRTEM (Fig. 2b), where no lattice fringes are recognized. The corresponding selected area

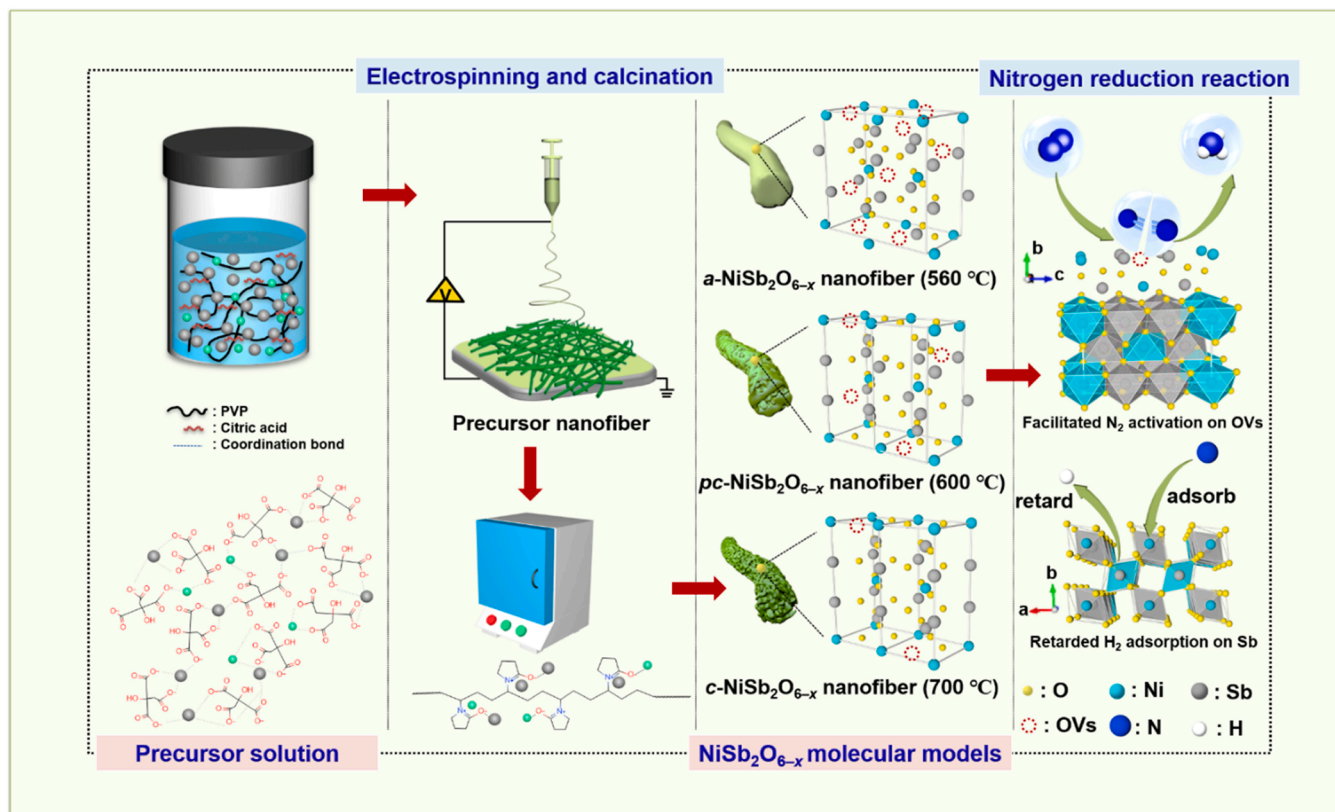
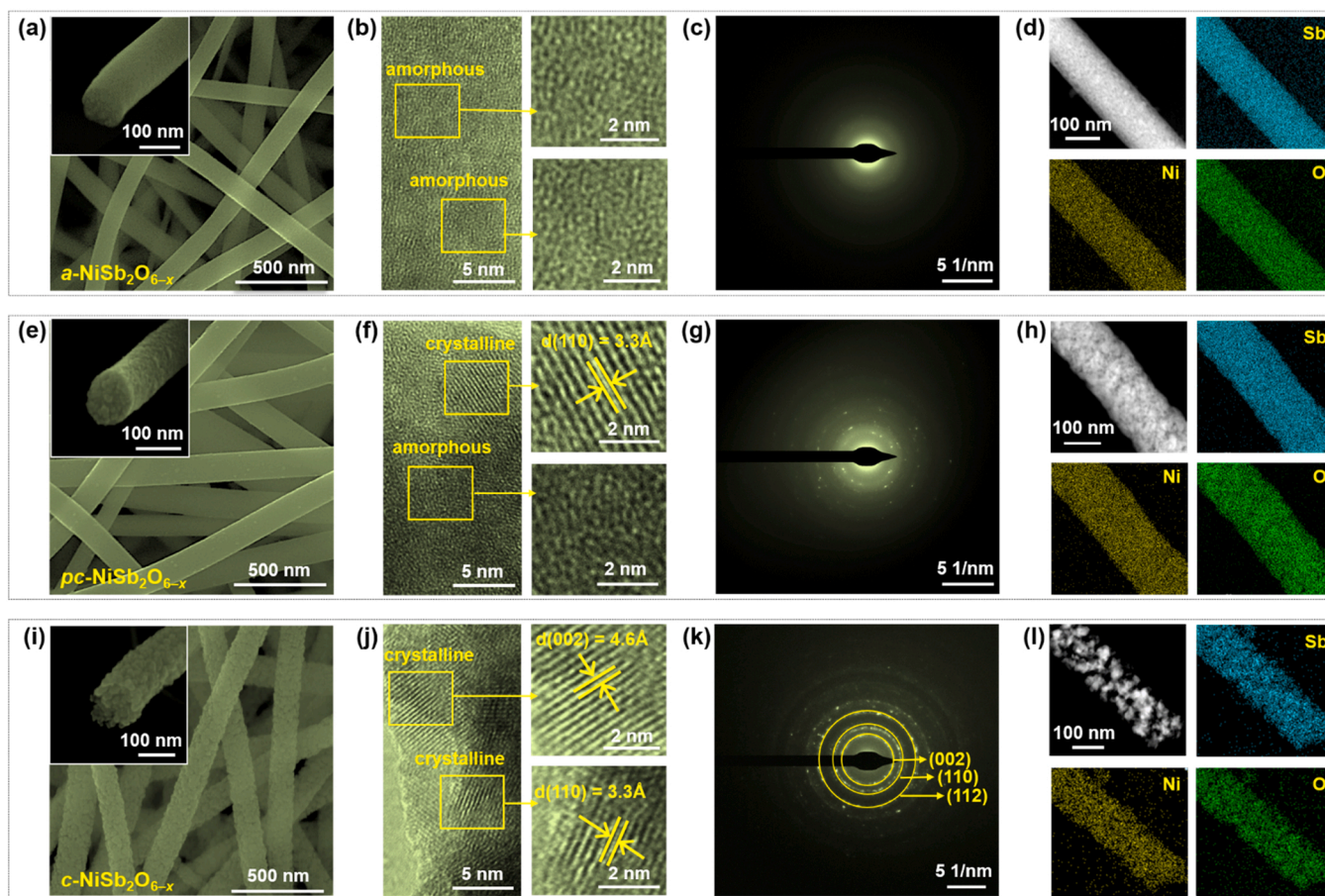


Fig. 1. Schematic diagram showing the process for the formation of  $\alpha\text{-NiSb}_2\text{O}_{6-x}$  nanofiber toward efficient  $\text{NH}_3$  synthesis through facilitated  $\text{N}_2$  activation and inhibited  $\text{H}_2$  adsorption.





**Fig. 2.** (a) SEM image, (b) HRTEM image, (c) SAED pattern and (d) STEM-EDX images of  $\alpha$ -NiSb<sub>2</sub>O<sub>6-x</sub> nanofiber. (e) SEM image, (f) HRTEM image, (g) SAED pattern and (h) STEM-EDX images of  $pc$ -NiSb<sub>2</sub>O<sub>6-x</sub> nanofiber. (i) SEM image, (j) HRTEM image, (k) SAED pattern and (l) STEM-EDX images of  $c$ -NiSb<sub>2</sub>O<sub>6-x</sub> nanofiber. The insets in (a), (e) and (i) show the SEM images of nanofiber tips.

electron diffraction (SAED) pattern exhibits blurry halation, confirming the amorphous nature of this nanofiber (Fig. 2c). When the calcination temperature increased to 600 °C, small grains began to occur since this temperature was high enough to enable nucleation and crystallization. Therefore, the surface is much rougher and the inner structure is composed of loosely packed grains, as shown in the TEM image of the  $pc$ -NiSb<sub>2</sub>O<sub>6-x</sub> nanofiber (Fig. 2e). As seen from the HRTEM image (Fig. 2f), small grains with parallel lattice fringes can be clearly seen, and the interplanar distance of 3.3 Å points to the (110) plane of trirutile-type NiSb<sub>2</sub>O<sub>6</sub> [55]. Moreover, Fig. 2f also shows amorphous zones existing at the grain boundaries. As for the SAED pattern of this nanofiber (Fig. 2g), diffraction spots can be distinguished from the blurry halation, which confirm the occurrence of crystal phase in the  $pc$ -NiSb<sub>2</sub>O<sub>6-x</sub> nanofiber. Calcination of the precursor nanofiber at 700 °C resulted in the formation of the  $c$ -NiSb<sub>2</sub>O<sub>6-x</sub> nanofiber (Fig. 2i), which has the roughest surface composed of larger-sized crystallites formed by the inter-grain transport and aggregation because of their different surface energies, owing to the Ostwald ripening effect [56]. Interplanar distances of 3.3 and 4.6 Å are ascribed to the (110) and (002) planes of NiSb<sub>2</sub>O<sub>6</sub> phase (Fig. 2j), suggesting the phase purity of the  $c$ -NiSb<sub>2</sub>O<sub>6-x</sub> nanofiber [55]. Fig. 2k presents its SAED pattern, in which the diffraction rings can be indexed to the (001), (110) and (112) planes of trirutile-type NiSb<sub>2</sub>O<sub>6</sub>, indicating a polycrystalline nature [57]. Fig. 2d, h and g present the scanning transmission electron microscopy (STEM) images of the three kinds of nanofibers, and the corresponding energy-dispersive X-ray (EDX) spectra. It can be seen that all nanofibers consist homogeneously of Sb, Ni and O elements; however, the microstructure gets rougher and looser with the increase of crystallinity. This

is the reason why the  $c$ -NiSb<sub>2</sub>O<sub>6-x</sub> nanofiber was brittle and weak in the mechanical properties, while the  $\alpha$ -NiSb<sub>2</sub>O<sub>6-x</sub> nanofiber was strong and flexible, and could be bent to a large extent owing to the uniform and dense alignment of the fine colloid particles (Fig. S3).

The phase evolution from  $\alpha$ -NiSb<sub>2</sub>O<sub>6-x</sub> to  $c$ -NiSb<sub>2</sub>O<sub>6-x</sub> nanofiber was further examined by XRD, as shown in Fig. 3a. For the  $c$ -NiSb<sub>2</sub>O<sub>6-x</sub> nanofiber, the diffraction peaks at 19.2°, 27.1°, 35.0°, 39.0°, 40.2°, 53.2°, 56.0°, 60.6°, 63.3°, 67.7°, 74.3°, 80.9° and 83.1° are attributed to the (002), (110), (103), (004), (113), (213), (220), (301), (310), (303), (321), (323) and (400) planes of trirutile-type NiSb<sub>2</sub>O<sub>6</sub> with  $P42_1nmn$  space group (PDF #38-1083) [57]. Besides, no diffraction peaks of NiO or Sb<sub>2</sub>O<sub>4</sub> can be found in this XRD pattern (Fig. S4), which indicates this nanofiber is composed of pure NiSb<sub>2</sub>O<sub>6</sub> phase instead of being a composite of NiO and Sb<sub>2</sub>O<sub>4</sub>. As for the  $pc$ -NiSb<sub>2</sub>O<sub>6-x</sub> nanofiber, although these diffraction peaks are still distinguishable, their intensities are obviously weakened owing to reduced crystallinity compared to  $c$ -NiSb<sub>2</sub>O<sub>6-x</sub>. By sharp contrast, no diffraction peaks can be found in the XRD pattern of the  $\alpha$ -NiSb<sub>2</sub>O<sub>6-x</sub> nanofiber, which is another proof of its amorphous nature. It is believed that amorphization can induce abundant OV's compared to the crystalline counterparts, which is beneficial to the electrochemical performance. To testify this expectation, Raman spectroscopy was conducted which is effective on determining the effect of defects on the local structure of NiSb<sub>2</sub>O<sub>6</sub> [58]. As shown in Fig. 3b, the band in the range of 500–600 cm<sup>-1</sup> is dominated by the elongation mode of the Sb—O<sub>cyt</sub> bonds, while those in the range of 600–800 cm<sup>-1</sup> are ascribed to the stretching modes of the Sb—O<sub>p</sub> bonds [59]. All nanofibers have nearly identical spectra, while the band positions downshift from  $c$ -NiSb<sub>2</sub>O<sub>6-x</sub> to  $\alpha$ -NiSb<sub>2</sub>O<sub>6-x</sub>, suggesting changed bond length and

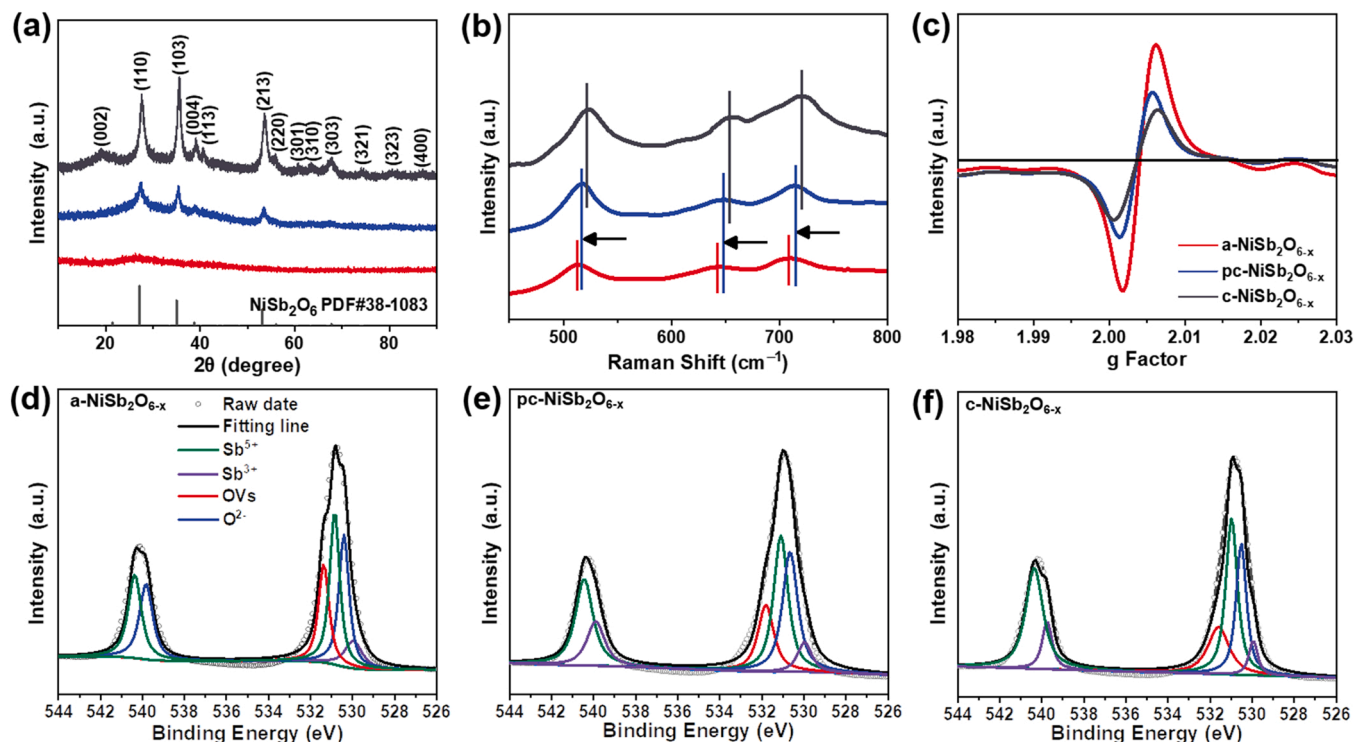


**Fig. 3.** (a) XRD patterns, (b) Raman spectra, and (c) EPR spectra of  $\alpha$ -NiSb<sub>2</sub>O<sub>6-x</sub>,  $pc$ -NiSb<sub>2</sub>O<sub>6-x</sub> and  $c$ -NiSb<sub>2</sub>O<sub>6-x</sub> nanofibers. Sb 3d XPS spectra of (d)  $\alpha$ -NiSb<sub>2</sub>O<sub>6-x</sub>, (e)  $pc$ -NiSb<sub>2</sub>O<sub>6-x</sub> and (f)  $c$ -NiSb<sub>2</sub>O<sub>6-x</sub> nanofibers.

angle, as well as increased disorder degree. In result, the disordered structure is accompanied by the generation of OV and under-coordinated dangling bonds, endowing  $\alpha$ -NiSb<sub>2</sub>O<sub>6-x</sub> with more active sites than the crystalline counterparts. Moreover, the three kinds of nanofibers were probed by EPR to measure the unpaired electrons, which are proportionally related to the quantities of OV and under-coordinated dangling bonds. Fig. 3c shows the EPR spectra, in which the signal intensity at  $g = 2.006$  increases progressively along with the decrease of crystallinity, demonstrating increased OV content from  $c$ -NiSb<sub>2</sub>O<sub>6-x</sub> to  $\alpha$ -NiSb<sub>2</sub>O<sub>6-x</sub>.

The chemical composition and states of the three kinds of nanofibers were compared by XPS. Since the binding energy of Sb 3d<sub>5/2</sub> is overlapped with that of O 1s, the Sb 3d XPS spectra are presented which include the O 1s spectra, as shown in Fig. 3d–f. The two peaks at 530.4 eV and 531.4 eV belong to O 1s, with the former corresponding to lattice oxygen and the latter corresponding to OVs [60]. The fitted OV area of  $\alpha$ -NiSb<sub>2</sub>O<sub>6-x</sub> is remarkably higher than that of  $pc$ -NiSb<sub>2</sub>O<sub>6-x</sub> or  $c$ -NiSb<sub>2</sub>O<sub>6-x</sub>, suggesting that amorphization can indeed induce more OVs. The two peaks at 540.5 eV (Sb 3d<sub>3/2</sub>) and 530.9 eV (Sb 3d<sub>5/2</sub>) are in accordance with Sb<sup>5+</sup> [61]. At the same time, the two peaks at 539.7 eV and 529.9 eV indicate the formation of Sb species with a lower valence state (Sb<sup>3+</sup>) on the surface of the samples [62]. The presence of lower-valence Sb<sup>3+</sup> means the generation of OVs, and the relative atomic ratio of Sb<sup>3+</sup>/Sb<sup>5+</sup> can also be used to estimate the OV content. A higher Sb<sup>3+</sup>/Sb<sup>5+</sup> ratio is witnessed in  $\alpha$ -NiSb<sub>2</sub>O<sub>6-x</sub> than that in  $pc$ -NiSb<sub>2</sub>O<sub>6-x</sub> or  $c$ -NiSb<sub>2</sub>O<sub>6-x</sub>, further proving that the former possesses more OVs. As for the Ni 2p spectra (Fig. S5), the two shake-up type peaks at 879.9 eV and 861.9 eV are indicative of the satellite peaks of Ni<sup>2+</sup>, respectively. Besides, the two peaks at 873.4 eV and 855.9 eV are attributed to the Ni<sup>2+</sup> 2p<sub>1/2</sub> and 2p<sub>3/2</sub> orbitals, and they shift slightly toward higher binding energies owing to amorphization [57]. The BET surface areas of the three kinds of nanofibers are given in Fig. S6, in which the  $\alpha$ -NiSb<sub>2</sub>O<sub>6-x</sub> nanofiber (92.64 m<sup>2</sup> g<sup>-1</sup>) is significantly larger than both  $pc$ -NiSb<sub>2</sub>O<sub>6-x</sub> nanofiber (53.98 m<sup>2</sup> g<sup>-1</sup>) and  $c$ -NiSb<sub>2</sub>O<sub>6-x</sub> nanofiber (32.51 m<sup>2</sup> g<sup>-1</sup>), which is beneficial for exposing more active

sites and facilitating the H<sup>+</sup>/e<sup>-</sup> transport.

### 3.2. Electrocatalytic NRR performance of amorphous NiSb<sub>2</sub>O<sub>6-x</sub> nanofiber

The NRR performance of the  $\alpha$ -NiSb<sub>2</sub>O<sub>6-x</sub> nanofiber was tested by electrolyzing in an H-type electrolysis cell, which was filled with a neutral electrolyte of 0.1 M Na<sub>2</sub>SO<sub>4</sub>. The linear sweep voltammetry (LSV) curves in N<sub>2</sub> and Ar are displayed in Fig. S7. It can be seen that the current density differs obviously in the N<sub>2</sub>-saturated electrolyte from in the Ar-saturated electrolyte, which probably derived from NRR in the N<sub>2</sub> atmosphere. The produced NH<sub>3</sub> was spectrophotometrically determined by using the indophenol blue method [40], and the calibration curve of standard NH<sub>3</sub> concentration and the UV–vis absorbance at 660 nm is provided in Fig. S8. The linear relationship between NH<sub>3</sub> concentration and UV–vis absorbance was obtained from the above calibration curve, according to which the NH<sub>3</sub> yield and FE at each potential could be calculated. Fig. S9 presents the chronoamperometric curves and the corresponding UV–vis absorption spectra of the stained electrolytes within the potential range of -0.15 to -0.55 V vs. RHE. Based on these data, the NH<sub>3</sub> yield and FE at each potential are shown in Fig. 4a. The highest FE of 23.3% is achieved at -0.25 V vs. RHE, while the maximum NH<sub>3</sub> yield of 6.8  $\mu$ g h<sup>-1</sup> mg<sup>-1</sup> is achieved at -0.3 V vs. RHE. To verify the validity of these values, ion chromatography (IC) as another quantification technique was employed, and the tiny deviation (<7%) in NH<sub>3</sub> yield between the two methods falls well within the uncertainty (Fig. S10). Note that these values significantly outperform those of either component, i.e., NiO nanofiber (2.4  $\mu$ g h<sup>-1</sup> mg<sup>-1</sup>, 6.0%) and Sb<sub>2</sub>O<sub>4</sub> nanofiber (1.5  $\mu$ g h<sup>-1</sup> mg<sup>-1</sup>, 8.7%), demonstrating the synergistic catalysis pathway between Ni and Sb (Fig. S11). The  $\alpha$ -NiSb<sub>2</sub>O<sub>6-x</sub> nanofiber was further subjected to a cycling experiment with alternating 2 h cycles between N<sub>2</sub>- and Ar-saturated electrolytes (Fig. 4b). It can be seen that NH<sub>3</sub> was produced with fairly stable yield and FE when electrolyzed in N<sub>2</sub>, while no traces could be detected in Ar. The chronoamperometric curve shown in Fig. 4c indicates that the  $\alpha$ -NiSb<sub>2</sub>O<sub>6-x</sub> nanofiber could



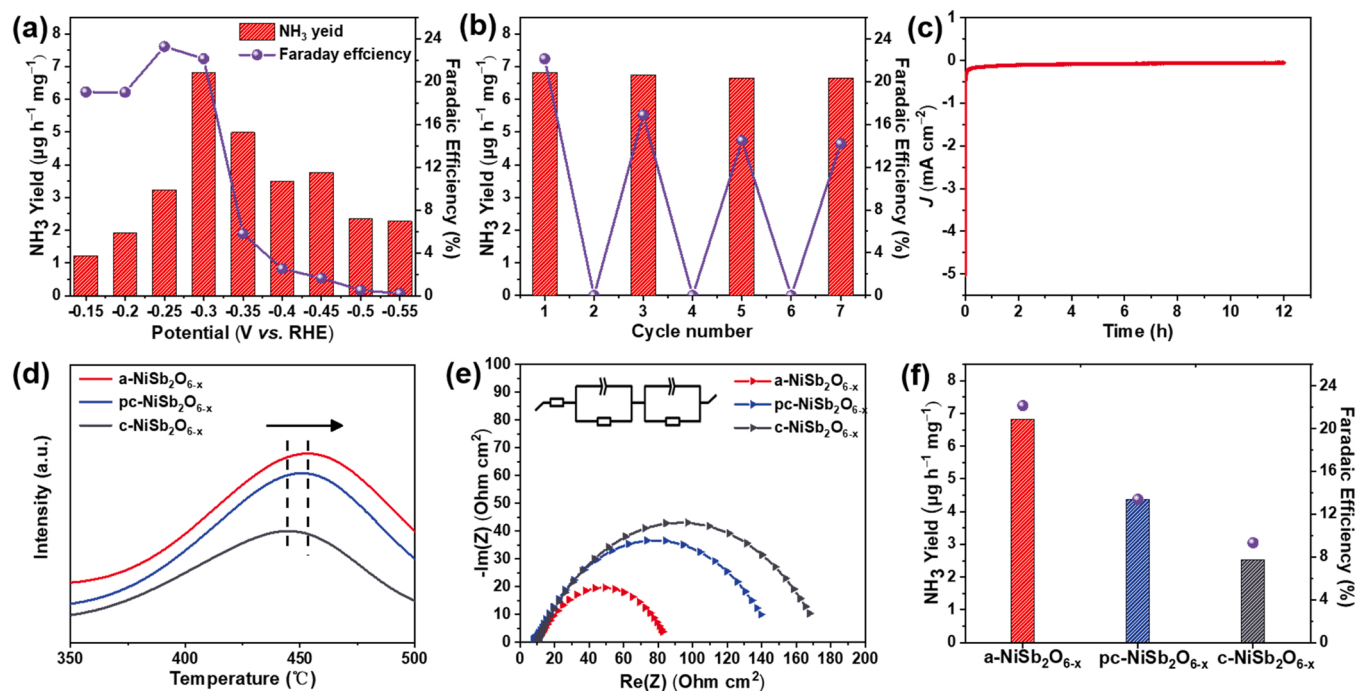


**Fig. 4.** (a)  $\text{NH}_3$  yield and FE of  $a\text{-NiSb}_2\text{O}_{6-x}$  nanofiber at each potential. (b)  $\text{NH}_3$  yield and FE of  $a\text{-NiSb}_2\text{O}_{6-x}$  nanofiber in alternating  $\text{N}_2$  and Ar atmosphere at  $-0.3$  V vs. RHE for 2 h. (c) Chronoamperometry curve of  $a\text{-NiSb}_2\text{O}_{6-x}$  nanofiber at  $-0.3$  V vs. RHE for 12 h. (d)  $\text{N}_2$ -TPD curves and (e) Nyquist plots of  $a\text{-NiSb}_2\text{O}_{6-x}$ ,  $pc\text{-NiSb}_2\text{O}_{6-x}$  and  $c\text{-NiSb}_2\text{O}_{6-x}$  nanofibers. (f)  $\text{NH}_3$  yield and FE of  $a\text{-NiSb}_2\text{O}_{6-x}$ ,  $pc\text{-NiSb}_2\text{O}_{6-x}$  and  $c\text{-NiSb}_2\text{O}_{6-x}$  nanofibers at  $-0.3$  V vs. RHE. The inset in (e) shows the corresponding equivalent circuit.

stably run for at least 12 h with negligible variation in the current density, confirming its long-term durability which is particularly crucial for practical applications. After the durability test, the  $a\text{-NiSb}_2\text{O}_{6-x}$  nanofiber was collected from the working electrode by sonication in ethanol, and dropped on a Cu grid for TEM characterization (Fig. S12). It can be seen that the fibrous morphology and amorphous nature of the  $a\text{-NiSb}_2\text{O}_{6-x}$  nanofiber were well retained without obvious alteration. To clarify the origin of  $\text{NH}_3$ , electrolysis was conducted in  $\text{N}_2$  under open circuit, or in Ar at  $-0.3$  V vs. RHE. As shown in Fig. S13, no  $\text{NH}_3$  could be detected under these conditions, confirming it was indeed produced through the electroreduction of  $\text{N}_2$  by the catalysis of the  $a\text{-NiSb}_2\text{O}_{6-x}$  nanofiber. Furthermore, possible byproducts  $\text{N}_2\text{H}_4$  and  $\text{NO}_2^-$  were also spectrophotometrically determined, and the calibration curves are provided in Figs. S14 and S15. It can be seen from Figs. S16 and S17 that the electrolyte after 2 h electrolysis did not contain any  $\text{N}_2\text{H}_4$  or  $\text{NO}_2^-$ , which demonstrates that the  $a\text{-NiSb}_2\text{O}_{6-x}$  nanofiber exhibited excellent selectivity towards  $\text{NH}_3$ . Moreover, the isotopic labeling was employed in which the electrolyte fed with  $^{15}\text{N}_2$  was subjected to electrocatalysis of the  $a\text{-NiSb}_2\text{O}_{6-x}$  nanofiber for different time (12, 36 and 72 h), and examined by  $^1\text{H}$  nuclear magnetic resonance (NMR) spectroscopy [40]. As seen from Fig. S18, two peaks corresponding to the resonance between  $^1\text{H}$  and  $^{15}\text{N}$  occur, and the peak area is linearly related to the electrolysis time, which indicate that the produced  $\text{NH}_3$  originated from the  $^{15}\text{N}_2$  feed gas rather than from the environmental contaminant [65].

As revealed in Fig. 4d, the NRR performance of the  $a\text{-NiSb}_2\text{O}_{6-x}$  nanofiber at  $-0.30$  V vs. RHE significantly outperforms its crystalline counterparts, including  $pc\text{-NiSb}_2\text{O}_{6-x}$  nanofiber ( $4.4 \mu\text{g h}^{-1} \text{mg}^{-1}$ , 13.4%) and  $c\text{-NiSb}_2\text{O}_{6-x}$  nanofiber ( $2.5 \mu\text{g h}^{-1} \text{mg}^{-1}$ , 9.3%), which reflects the superiority of amorphous materials over their crystalline counterparts. To understand the underlying reason of this phenomenon, the  $\text{N}_2$ -TPD experiment was carried out on the three kinds of nanofibers. As displayed in Fig. 4e, the strong peak at around  $450^\circ\text{C}$  is assigned to the  $\text{N}_2$  chemisorption. It is apparent that the  $a\text{-NiSb}_2\text{O}_{6-x}$  nanofiber shows a more positive and stronger chemisorption peak than  $pc\text{-NiSb}_2\text{O}_{6-x}$  and  $c\text{-NiSb}_2\text{O}_{6-x}$ , illustrating the substantial increase of

adsorption capacity for  $\text{N}_2$  molecules [63,64]. The charge transfer ability is another crucial factor to determine the NRR performance of an electrocatalyst. Thus, the electrochemical impedance spectroscopy (EIS) was conducted to investigate the charge transfer abilities of the three kinds of nanofibers. According to the fitted results provided in Fig. 4f, the  $a\text{-NiSb}_2\text{O}_{6-x}$  nanofiber has the smallest semicircle diameter corresponding to the lowest charge transfer resistance ( $R_{ct}$ ), which might be attributed to the highest VO content of the amorphous structure that compensates the negative impact of trapping carriers.

### 3.3. DFT-based reaction mechanism of amorphous $\text{NiSb}_2\text{O}_{6-x}$ nanofiber

DFT calculations were performed to theoretically understand the mechanism of the superior NRR performance of the  $a\text{-NiSb}_2\text{O}_{6-x}$  nanofiber over its crystalline counterparts. As the initial and a crucial step, the adsorption behaviors of  $\text{N}_2$  on  $a\text{-NiSb}_2\text{O}_{6-x}$ ,  $pc\text{-NiSb}_2\text{O}_{6-x}$  and  $c\text{-NiSb}_2\text{O}_{6-x}$  were studied. To identify the most stable adsorption structures on the three kinds of models, we considered different adsorption configurations as shown in Fig. S19. Compared with  $pc\text{-NiSb}_2\text{O}_{6-x}$  ( $-0.19$  eV) and  $c\text{-NiSb}_2\text{O}_{6-x}$  ( $-0.12$  eV), the most stable adsorption structure of  $\text{N}_2$  on  $a\text{-NiSb}_2\text{O}_{6-x}$  exhibits a much lower binding energy ( $-0.27$  eV), indicating the strongest adsorption ability of  $a\text{-NiSb}_2\text{O}_{6-x}$  toward  $\text{N}_2$ . Moreover, the electronic structure analysis was carried out to unravel the adsorption trend, and the density of states (DOS) are shown in Fig. S20. It is found that with the increase of VO concentration, the electronic states of both Ni and Sb near the Fermi level are increased from  $c\text{-NiSb}_2\text{O}_{6-x}$  to  $a\text{-NiSb}_2\text{O}_{6-x}$ . The new states are highly active and can overlap more with the orbitals of  $\text{N}_2$ , which can serve as electron-trapping regions to facilitate the adsorption and the subsequent activation of  $\text{N}_2$ , as well as enable high-speed electron transfer during the NRR process. The total free-energy profiles and the corresponding optimized structures for each step are provided in Fig. 5, and the energy change for each step is presented in Fig. S21. DFT calculations reveal that the reduction of  $^*\text{NH}_2$  to  $^*\text{NH}_3$  is the most energetically uphill step for all the three kinds of models, which means the potential-determining

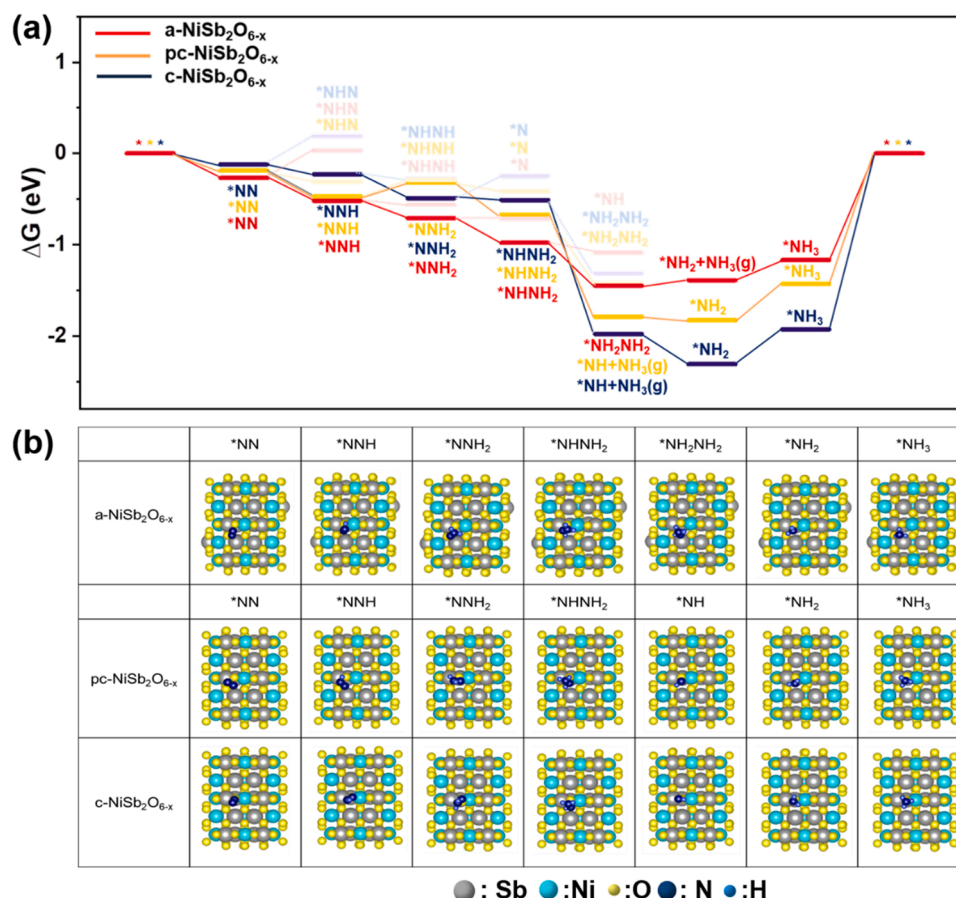


**Fig. 5.** (a) DFT-based free-energy profiles and (b) optimized structures (top view) of the intermediates for N<sub>2</sub> adsorption and activation on *a*-NiSb<sub>2</sub>O<sub>6-x</sub>, *pc*-NiSb<sub>2</sub>O<sub>6-x</sub> and *c*-NiSb<sub>2</sub>O<sub>6-x</sub> respectively.

step (PDS) is the formation of the second NH<sub>3</sub> molecule. The PDS energy barrier of *a*-NiSb<sub>2</sub>O<sub>6-x</sub> is significantly reduced to only 0.22 eV compared to that of *pc*-NiSb<sub>2</sub>O<sub>6-x</sub> (0.4 eV) and *c*-NiSb<sub>2</sub>O<sub>6-x</sub> (0.38 eV). In other words, *a*-NiSb<sub>2</sub>O<sub>6-x</sub> shows the highest activity toward N<sub>2</sub> reduction, which is believed to originate from amorphization. In the last step, *a*-NiSb<sub>2</sub>O<sub>6-x</sub> also shows the lowest energy barrier for the dissociation of NH<sub>3</sub>, implying the generated NH<sub>3</sub> molecule is more easily to be released from the surface of *a*-NiSb<sub>2</sub>O<sub>6-x</sub> than from *pc*-NiSb<sub>2</sub>O<sub>6-x</sub> and *c*-NiSb<sub>2</sub>O<sub>6-x</sub>. Moreover, all the intermediates are adsorbed at the bridge site or the hollow site of Ni and Sb atoms. From the calculation results, it can be concluded that *a*-NiSb<sub>2</sub>O<sub>6-x</sub> is more liable for N<sub>2</sub> adsorption and activation as well as NH<sub>3</sub> release, owing to the synergistic catalysis pathway between Ni and Sb.

#### 4. Conclusions

In summary, an amorphous NiSb<sub>2</sub>O<sub>6-x</sub> nanofiber is synthesized in which Ni and Sb contribute to a synergistic catalysis pathway for inhibiting the two-electron transfer process of HER as well as activating the adsorbed N<sub>2</sub> molecules. To further promote the NRR performance, a new strategy of amorphization is developed which is expected to produce more oxygen vacancies (OVs) and under-coordinated dangling bonds to mimic the “π back-donation” behavior. Benefiting from the synergistic superiority between coupled element design and amorphization strategy, the amorphous NiSb<sub>2</sub>O<sub>6-x</sub> nanofiber outperforms either component (NiO or Sb<sub>2</sub>O<sub>4</sub>) as well as its crystalline counterparts in terms of NH<sub>3</sub> yield and FE, whose underlying mechanism is explored by means of DFT calculations. In this sense, our work represents a successful attempt to design efficient electrocatalysts for NH<sub>3</sub> synthesis.

#### CRediT authorship contribution statement

**Wanping Xu:** Investigation, Writing – original draft. **Meng Zhang:** Investigation. **Chunlan Ma:** Software. **Shuhong Wu:** Validation. **Yi-Tao Liu:** Conceptualization, Supervision, Writing – review & editing, Project administration, Funding acquisition.

#### Declaration of Competing Interest

The authors declare that they have no known competing financial interests or personal relationships that could have appeared to influence the work reported in this paper.

#### Acknowledgements

This work was financially supported by the National Natural Science Foundation of China (No. 52173055), the Natural Science Foundation of Shanghai (No. 19ZR1401100), the Fundamental Research Funds for the Central Universities and DHU Distinguished Young Professor Program (No. LZA2020001).

#### Appendix A. Supporting information

Supplementary data associated with this article can be found in the online version at [doi:10.1016/j.apcatb.2022.121225](https://doi.org/10.1016/j.apcatb.2022.121225).

## References

- [1] Y. Li, H. Wang, C. Priest, S. Li, P. Xu, G. Wu, Advanced electrocatalysis for energy and environmental sustainability via water and nitrogen reactions, *Adv. Mater.* 33 (2020), 2000381.
- [2] L. Shi, Y. Yin, S. Wang, X. Xu, H. Wu, J. Zhang, S. Wang, H. Sun, Rigorous and reliable operations for electrocatalytic nitrogen reduction, *Appl. Catal. B Environ.* 278 (2020), 119325.
- [3] B.H.R. Suryanto, H.-L. Du, D. Wang, J. Chen, A.N. Simonov, D.R. MacFarlane, Challenges and prospects in the catalysis of electroreduction of nitrogen to ammonia, *Nat. Catal.* 2 (2019) 290–296.
- [4] W. Guo, K. Zhang, Z. Liang, R. Zou, Q. Xu, Electrochemical nitrogen fixation and utilization: theories, advanced catalyst materials and system design, *Chem. Soc. Rev.* 48 (2019) 5658–5716.
- [5] M. L  gar  , G. B  langer-Chabot, R.D. Dewhurst, E. Welz, I. Krummenacher, B. Engels, H. Braunschweig, Nitrogen fixation and reduction at boron, *Science* 359 (2018) 896–900.
- [6] H. Tao, C. Choi, L.-X. Ding, Z. Jiang, Z. Han, M. Jia, Q. Fan, Y. Gao, H. Wang, A. W. Robertson, S. Hong, Y. Jung, S. Liu, Z. Sun, Nitrogen fixation by Ru single-atom electrocatalytic reduction, *Chem* 5 (2019) 204–214.
- [7] J. Zheng, F. Liao, S. Wu, G. Jones, T.-Y. Chen, J. Fellowes, T. Sudmeier, I. J. McPherson, I. Wilkinson, S.C.E. Tsang, Efficient non-dissociative activation of dinitrogen to ammonia over lithium-promoted ruthenium nanoparticles at low pressure, *Angew. Chem. Int. Ed.* 58 (2019) 17335–17341.
- [8] C. Yang, B. Huang, S. Bai, Y. Feng, Q. Shao, X. Huang, A generalized surface chalcogenation strategy for boosting the electrochemical N<sub>2</sub> fixation of metal nanocrystals, *Adv. Mater.* 32 (2020), 2001267.
- [9] Y. Deng, Z. Xiao, Z. Wang, J. Lai, X. Liu, D. Zhang, Y. Han, S. Li, W. Sun, L. Wang, The rational adjusting of proton-feeding by Pt-doped FeP/C hollow nanorod for promoting nitrogen reduction kinetics, *Appl. Catal. B Environ.* 291 (2021), 120047.
- [10] L. Zhang, X. Ji, X. Ren, Y. Ma, X. Shi, Z. Tian, A.M. Asiri, L. Chen, B. Tang, X. Sun, Electrochemical ammonia synthesis via nitrogen reduction reaction on a MoS<sub>2</sub> catalyst: theoretical and experimental studies, *Adv. Mater.* 30 (2018), 1800191.
- [11] Q. Li, Y. Guo, Y. Tian, W. Liu, K. Chu, Activating VS<sub>2</sub> basal planes for enhanced NRR electrocatalysis: the synergistic role of S-vacancies and B dopants, *J. Mater. Chem. A* 8 (2020) 16195–16202.
- [12] J. Wang, H. Nan, Y. Tian, K. Chu, FeMo<sub>3</sub>S<sub>4</sub> for efficient nitrogen reduction reaction, *ACS Sustain. Chem. Eng.* 8 (2020) 12733–12740.
- [13] X. Zi, J. Wan, X. Yang, W. Tian, H. Zhang, Y. Wang, Vacancy-rich 1T-MoS<sub>2</sub> monolayer confined to MoO<sub>3</sub> matrix: an interface-engineered hybrid for efficiently electrocatalytic conversion of nitrogen to ammonia, *Appl. Catal. B Environ.* 286 (2021), 119870.
- [14] P.-Y. Liu, K. Shi, W.-Z. Chen, R. Gao, Z.-L. Liu, H. Hao, Y.-Q. Wang, Enhanced electrocatalytic nitrogen reduction reaction performance by interfacial engineering of MOF-based sulfides FeNi<sub>2</sub>S<sub>4</sub>/NiS hetero-interface, *Appl. Catal. B Environ.* 287 (2021), 119956.
- [15] X. Yang, J. Nash, J. Anibal, M. Dunwell, S. Kattel, E. Stavitski, K. Attenkofer, J. G. Chen, Y. Yan, B. Xu, Mechanistic insights into electrochemical nitrogen reduction reaction on vanadium nitride nanoparticles, *J. Am. Chem. Soc.* 140 (2018) 13387–13391.
- [16] X. Ren, G. Cui, L. Chen, F. Xie, Q. Wei, Z. Tian, X. Sun, Electrochemical N<sub>2</sub> fixation to NH<sub>3</sub> under ambient conditions: Mo<sub>2</sub>N nanorod as a highly efficient and selective catalyst, *Chem. Commun.* 54 (2018) 8474–8477.
- [17] X. Yang, S. Kattel, J. Nash, X. Chang, J.H. Lee, Y. Yan, J.G. Chen, B. Xu, Quantification of active sites and elucidation of the reaction mechanism of the electrochemical nitrogen reduction reaction on vanadium nitride, *Angew. Chem. Int. Ed.* 58 (2019) 13768–13772.
- [18] Y. Du, C. Jiang, L. Song, B. Gao, H. Gong, W. Xia, L. Sheng, T. Wang, J. He, Regulating surface state of WO<sub>3</sub> nanosheets by gamma irradiation for suppressing hydrogen evolution reaction in electrochemical N<sub>2</sub> fixation, *Nano Res.* 13 (2020) 2784–2790.
- [19] J. Song, J. Dai, P. Zhang, Y. Liu, J. Yu, B. Ding, g-C<sub>3</sub>N<sub>4</sub> encapsulated ZrO<sub>2</sub> nanofibrous membrane decorated with CdS quantum dots: a hierarchically structured, self-supported electrocatalyst toward synergistic NH<sub>3</sub> synthesis, *Nano Res.* 14 (2021) 1479–1487.
- [20] X. Hu, Y. Sun, S. Guo, J. Sun, Y. Fu, S. Chen, S. Zhang, J. Zhu, Identifying electrocatalytic activity and mechanism of Ce<sub>1/3</sub>NbO<sub>3</sub> perovskite for nitrogen reduction to ammonia at ambient conditions, *Appl. Catal. B Environ.* 280 (2021), 119419.
- [21] H. Cheng, L.-X. Ding, G.-F. Chen, L. Zhang, J. Xue, H. Wang, Molybdenum carbide nanodots enable efficient electrocatalytic nitrogen fixation under ambient conditions, *Adv. Mater.* 30 (2018), 1803694.
- [22] H. Cheng, P. Cui, F. Wang, L.-X. Ding, H. Wang, High efficiency electrochemical nitrogen fixation achieved with a lower pressure reaction system by changing the chemical equilibrium, *Angew. Chem. Int. Ed.* 58 (2019) 15541–15547.
- [23] Y. Ma, T. Yang, H. Zou, W. Zang, Z. Kou, L. Mao, Y. Feng, L. Shen, S.J. Pennycook, L. Duan, X. Li, J. Wang, Synergizing Mo single atoms and Mo<sub>2</sub>C nanoparticles on CNTs synchronizes selectivity and activity of electrocatalytic N<sub>2</sub> reduction to ammonia, *Adv. Mater.* 32 (2020), 2002177.
- [24] D. Yan, H. Li, C. Chen, Y. Zou, S. Wang, Defect engineering strategies for nitrogen reduction reactions under ambient conditions, *Small Methods* 3 (2018) 1800331–1808744.
- [25] Q. Wang, Y. Lei, D. Wang, Y. Li, Defect engineering in earth-abundant electrocatalysts for CO<sub>2</sub> and N<sub>2</sub> reduction, *Energy Environ. Sci.* 12 (2019) 1730–1750.
- [26] N. Cao, Z. Chen, K. Zang, J. Xu, J. Zhong, J. Luo, X. Xu, G. Zheng, Doping strain induced bi-Ti<sup>3+</sup> pairs for efficient N<sub>2</sub> activation and electrocatalytic fixation, *Nat. Commun.* 10 (2019) 2877.
- [27] T. Wu, X. Zhu, Z. Xing, S. Mou, C. Li, Y. Qiao, Q. Liu, Y. Luo, X. Shi, Y. Zhang, X. Sun, Greatly improving electrochemical N<sub>2</sub> reduction over TiO<sub>2</sub> nanoparticles by iron doping, *Angew. Chem. Int. Ed.* 58 (2019) 18449–18453.
- [28] T. Wu, H. Zhao, X. Zhu, Z. Xing, Q. Liu, T. Liu, S. Gao, S. Lu, G. Chen, A.M. Asiri, Y. Zhang, X. Sun, Identifying the origin of Ti<sup>3+</sup> activity toward enhanced electrocatalytic N<sub>2</sub> reduction over TiO<sub>2</sub> nanoparticles modulated by mixed-valent copper, *Adv. Mater.* 32 (2020), 2000299.
- [29] K. Chu, Y. Liu, Y. Cheng, Q. Li, Synergistic boron-dopants and boron-induced oxygen vacancies in MnO<sub>2</sub> nanosheets to promote electrocatalytic nitrogen reduction, *J. Mater. Chem. A* 8 (2020) 5200–5208.
- [30] K. Chu, Y. Liu, Y. Li, Y. Guo, Y. Tian, H. Zhang, Multi-functional Mo-doping in MnO<sub>2</sub> nanoflowers toward efficient and robust electrocatalytic nitrogen fixation, *Appl. Catal. B Environ.* 264 (2020), 118525.
- [31] D.K. Yesudoss, G. Lee, S. Shanmugam, Strong catalyst support interactions in defect-rich γ-Mo<sub>2</sub>N nanoparticles loaded 2D-h-BN hybrid for highly selective nitrogen reduction reaction, *Appl. Catal. B Environ.* 287 (2021), 119952.
- [32] M. Zhang, Y. Wang, Y. Zhang, J. Song, Y. Si, J. Yan, C. Ma, Y.-T. Liu, J. Yu, B. Ding, Conductive and elastic TiO<sub>2</sub> nanofibrous aerogels: a new concept toward self-supported electrocatalysts with superior activity and durability, *Angew. Chem. Int. Ed.* 59 (2020) 23252–23260.
- [33] Z. Han, C. Choi, S. Hong, T.-S. Wu, Y.-L. Soo, Y. Jung, J. Qiu, Z. Sun, Activated TiO<sub>2</sub> with tuned vacancy for efficient electrocatalytic nitrogen reduction, *Appl. Catal. B Environ.* 257 (2019), 117896.
- [34] K. Chu, Y. Luo, P. Shen, X. Li, Q. Li, Y. Guo, Unveiling the synergy of O-vacancy and heterostructure over MoO<sub>3-x</sub>/MXene for N<sub>2</sub> electroreduction to NH<sub>3</sub>, *Adv. Energy Mater.* 12 (2022), 2103022.
- [35] S.L. Foster, S.I.P. Bakovic, R.D. Duda, S. Maheshwari, R.D. Milton, S.D. Minter, M. J. Janik, J.N. Renner, L.F. Greenlee, Catalysts for nitrogen reduction to ammonia, *Nat. Catal.* 1 (2018) 490–500.
- [36] Y. Ren, C. Yu, X. Tan, H. Huang, Q. Wei, J. Qiu, Strategies to suppress hydrogen evolution for highly selective electrocatalytic nitrogen reduction: challenges and perspectives, *Energy Environ. Sci.* 14 (2021) 1176–1193.
- [37] Y.-C. Hao, Y. Guo, L.-W. Chen, M. Shu, X.-Y. Wang, T.-A. Bu, W.-Y. Gao, N. Zhang, X. Su, X. Feng, J.-W. Zhou, B. Wang, C.-W. Hu, A.-X. Yin, R. Si, Y.-W. Zhang, C.-H. Yan, Promoting nitrogen electroreduction to ammonia with bismuth nanocrystals and potassium cations in water, *Nat. Catal.* 2 (2019) 448–456.
- [38] Y. Wang, M. Shi, D. Bao, F. Meng, Q. Zhang, Y. Zhou, K. Liu, Y. Zhang, J. Wang, Z. Chen, D. Liu, Z. Jiang, M. Luo, L. Gu, Q. Zhang, X. Cao, Y. Yao, M. Shao, Y. Zhang, X.-B. Zhang, J.G. Chen, J. Yan, Q. Jiang, Generating defect-rich bismuth for enhancing the rate of nitrogen electroreduction to ammonia, *Angew. Chem. Int. Ed.* 58 (2019) 9464–9469.
- [39] L. Li, C. Tang, B. Xia, H. Jin, Y. Zheng, S.-Z. Qiao, Two-dimensional mosaic bismuth nanosheets for highly selective ambient electrocatalytic nitrogen reduction, *ACS Catal.* 9 (2019) 2902–2908.
- [40] Y.-T. Liu, D. Li, J. Yu, B. Ding, Stable confinement of black phosphorus quantum dots on black tin oxide nanotubes: a robust, double-active electrocatalyst toward efficient nitrogen fixation, *Angew. Chem. Int. Ed.* 58 (2019) 16439–16444.
- [41] Y.-T. Liu, L. Tang, J. Dai, J. Yu, B. Ding, Promoted electrocatalytic nitrogen fixation in Fe-Ni layered double hydroxide arrays coupled to carbon nanofibers: the role of phosphorus doping, *Angew. Chem. Int. Ed.* 59 (2020) 13623–13627.
- [42] C. Lv, L. Zhong, Y. Yao, D. Liu, Y. Kong, X. Jin, Z. Fang, W. Xu, K.N. Dinh, M. Shao, L. Song, G. Chen, S. Li, Q. Yan, G. Yu, Boosting electrocatalytic ammonia production through mimicking “π back-donation”, *Chem* 6 (2020) 2690–2702.
- [43] L. Li, C. Tang, X. Cui, Y. Zheng, X. Wang, H. Xu, S. Zhang, T. Shao, K. Davey, S.-Z. Qiao, Efficient nitrogen fixation to ammonia through integration of plasma oxidation with electrocatalytic reduction, *Angew. Chem. Int. Ed.* 60 (2021) 14131–14137.
- [44] J. Greeley, T.F. Jaramillo, J. Bonde, I. Chorkendorff, J.K. N  rskov, Computational high-throughput screening of electrocatalytic materials for hydrogen evolution, *Nat. Mater.* 5 (2006) 909–913.
- [45] L. Li, C. Tang, H. Jin, K. Davey, S.-Z. Qiao, Main-group elements boost electrochemical nitrogen fixation, *Chem* 7 (2021) 3232–3255.
- [46] X. Li, Y. Luo, Q. Li, Y. Guo, K. Chu, Constructing an electron-rich interface over an Sb/Nb<sub>2</sub>CT<sub>x</sub>-MXene heterojunction for enhanced electrocatalytic nitrogen reduction, *J. Mater. Chem. A* 9 (2021) 15955–15962.
- [47] K.P. Abhilash, L. Tang, M. Yang, Y. Ma, Q. Xia, Q. Guo, H. Xia, Research advances of amorphous metal oxides in electrochemical energy storage and conversion, *Small* 15 (2019), 1804371.
- [48] G. Kresse, J. Furthm  ller, Efficient iterative schemes for *ab initio* total-energy calculations using a plane-wave basis set, *Phys. Rev. B* 54 (1996) 11169–11186.
- [49] J.P. Perdew, K. Burke, M. Ernzerhof, Generalized gradient approximation made simple, *Phys. Rev. Lett.* 77 (1996) 3865–3868.
- [50] P.E. Bl  chl, Projector augmented-wave method, *Phys. Rev. B* 50 (1994) 17953–17979.
- [51] W.G. Rothchild, Binding of hydrogen donors by peptide groups of lactams. Identity of the interaction sites, *J. Am. Chem. Soc.* 94 (1972) 8676–8683.
- [52] H. Tsunoyama, N. Ichikuni, H. Sakurai, T. Tsukuda, Effect of electronic structures of Au clusters stabilized by poly(N-vinyl-2-pyrrolidone) on aerobic oxidation catalysis, *J. Am. Chem. Soc.* 131 (2009) 7086–7093.
- [53] K.M. Kozczur, S. Mourdikoudis, L. Polavarapu, E. Skrabalak, Polyvinylpyrrolidone (PVP) in nanoparticle synthesis, *Dalton Trans.* 44 (2015) 17883–17905.



- [54] S.-H. Choi, I.-S. Hwang, J.-H. Lee, S.-G. Oh, I.-D. Kim, Microstructural control and selective C<sub>2</sub>H<sub>5</sub>OH sensing properties of Zn<sub>2</sub>SnO<sub>4</sub> nanofibers prepared by electrospinning, *Chem. Commun.* 47 (2011) 9315–9317.
- [55] V.-M. Rodríguez-Betancourt, H.G. Bonilla, M.F. Martínez, A.G. Bonilla, J. P. Moran-Lazaro, J.T.G. Bonilla, M.A. González, M. de la Luz Olvera Amador, Gas sensing properties of NiSb<sub>2</sub>O<sub>6</sub> micro- and nanoparticles in propane and carbon monoxide atmospheres, *J. Nanomater.* 2017 (2017) 8792567–8792569.
- [56] L. Wang, L. Wang, X. Meng, F.-S. Xiao, New strategies for the preparation of sinter-resistant metal-nanoparticle-based catalysts, *Adv. Mater.* 31 (2019), 1901905.
- [57] J. Han, M. Xu, M. Jia, T. Liu, Evaluation of reduced graphene oxide-supported NiSb<sub>2</sub>O<sub>6</sub> nanocomposites for reversible lithium storage, *Ceram. Int.* 42 (2016) 14782–14787.
- [58] H. Haeuseler, Infrared and Raman spectra and normal coordinate calculations on trirutile-type compounds, *Spectrochim. Acta A Mol. Spectrosc.* 37 (1981) 487–495.
- [59] H. Zhang, K. Sun, Z. Feng, P. Ying, C. Li, Studies on the SbO<sub>x</sub> species of SbO<sub>x</sub>/SiO<sub>2</sub> catalysts for methane-selective oxidation to formaldehyde, *Appl. Catal. A Gen.* 305 (2006) 110–119.
- [60] A. Darwiche, L. Bodenes, L. Madec, L. Monconduit, H. Martinez, Impact of the salts and solvents on the SEI formation in Sb/Na batteries: an XPS analysis, *Electrochim. Acta* 207 (2016) 284–292.
- [61] A.N. Bondarchuk, I. Corrales-Mendoza, F. Marken, L.Á. Arellanes-Mendoza, J. A. Aguilar-Martínez, L.G. Silva-Vidaurre, G. Curiel-Olivares, F. Montejó-Alvaró, Hematite photoelectrodes grown on porous CuO–Sb<sub>2</sub>O<sub>5</sub>–SnO<sub>2</sub> ceramics for photoelectrochemical water splitting, *Sol. Energy Mater. Sol. Cells* 221 (2021), 110886.
- [62] J. Li, L. Han, X. Zhang, G. Zhu, T. Chen, T. Lu, L. Pan, Sb<sub>2</sub>O<sub>5</sub>/Co-containing carbon polyhedra as anode material for high-performance lithium-ion batteries, *Chem. Eng. J.* 370 (2019) 800–809.
- [63] P.-Y. Liu, K. Shi, W.-Z. Chen, R. Gao, Z.-L. Liu, H. Hao, Y.-Q. Wang, Enhanced electrocatalytic nitrogen reduction reaction performance by interfacial engineering of MOF-based sulfides FeNi<sub>2</sub>S<sub>4</sub>/NiS hetero-interface, *Appl. Catal. B Environ.* 287 (2021), 119956.
- [64] K. Chu, X. Li, Q. Li, Y. Guo, H. Zhang, Synergistic enhancement of electrocatalytic nitrogen reduction over boron nitride quantum dots decorated Nb<sub>2</sub>CT<sub>x</sub>-MXene, *Small* 17 (2021), 2102363.
- [65] Y. Meng, W. Song, H. Huang, Z. Ren, S.-Y. Chen, S.L. Suib, Structure-property relationship of bifunctional MnO<sub>2</sub> nanostructures: highly efficient, ultra-stable electrochemical water oxidation and oxygen reduction reaction catalysts identified in alkaline media, *J. Am. Chem. Soc.* 136 (2014) 11452–11464.